



**HAL**  
open science

## Experimental investigation of nozzle shape effect on wall shear stress beneath impinging round jet

B. Montagné, K Sadjavi, Pierre Bragança, Amina Meslem, Magdalena Kristiawan

### ► To cite this version:

B. Montagné, K Sadjavi, Pierre Bragança, Amina Meslem, Magdalena Kristiawan. Experimental investigation of nozzle shape effect on wall shear stress beneath impinging round jet. International Conference on Mechanics, Fluid Mechanics, Heat and Mass Transfer (MFMHMT 2014), Feb 2014, Interlaken, Switzerland. hal-01149948

**HAL Id: hal-01149948**

**<https://hal.science/hal-01149948>**

Submitted on 7 May 2015

**HAL** is a multi-disciplinary open access archive for the deposit and dissemination of scientific research documents, whether they are published or not. The documents may come from teaching and research institutions in France or abroad, or from public or private research centers.

L'archive ouverte pluridisciplinaire **HAL**, est destinée au dépôt et à la diffusion de documents scientifiques de niveau recherche, publiés ou non, émanant des établissements d'enseignement et de recherche français ou étrangers, des laboratoires publics ou privés.

# Experimental investigation of nozzle shape effect on wall shear stress beneath impinging round jet

B. Montagné, K. Sodjavi, P. Bragança, A. Meslem and M. Kristiawan

**Abstract**— This paper reports on measurements of velocities and wall shear rates for an impinging round jet. The test parameter that we consider is the nozzle shape. The Particle Image Velocimetry (PIV) was used to measure the axial and radial velocity components. The limitations of the PIV technique in the vicinity of the target wall are addressed by using the electrodiffusion technique to achieve wall shear rate distribution. A round orifice perforated either on a flat plate (RO/P) or on a hemispherical surface (RO/H), is compared to a reference convergent nozzle (CONV). All the nozzles have the same exit diameter  $D$ . The exit volumetric flow rate was also conserved and led to the same Reynolds number based on the exit bulk-velocity,  $Re_0 = 5290$ . The nozzle-to-wall distance was constant and equal to  $2D$ . The whole velocity field and wall shear rates in the three impinging round jets having different features are compared. This has improved the understanding of the jet/wall interaction. The wall shear rate is in a close relationship with the near field flow features, themselves affected by nozzle geometry. The orifice nozzles generate narrower exit profiles compared to the convergent nozzle. The *vena contracta* effect in orifice jets, more intense with RO/P than with RO/H, generates an increase of the exit centerline velocity. The hemispherical surface of RO/H nozzle leads to a *vena-stretching* attenuating somewhat the *vena contracta* effect at the jet exit. The instantaneous PIV fields indicated the formation of secondary vortices in the region where a secondary peak in the mean and rms distributions of wall shear rate emerged.

**Keywords**—Electrodiffusion, hemispherical nozzle, impinging round jet, PIV, wall shear rate.

## I. INTRODUCTION

A thorough research, beginning with Gardon et al. contributions [1-3], concerned the heat/mass transfer in impinging jets, and an early observation has been made in [2] about the importance of jet turbulence in heat transfer processes. It was shown that some seemingly anomalous heat-transfer phenomena can be explained as effects of the turbulence occurring in jets. Turbulence is generated by the jet itself and by external disturbances and varies significantly with the nozzle shape, upstream conditions and position within the jet. One decade after the observation of Gardon and Akrifat [2], Popiel and Boguslawski [4] claimed that nozzle exit configuration is the most important factor affecting the heat/mass transfer. Despite these first very significant

indications, there are only a few studies dedicated to heat/mass transfer dependency of nozzle geometry.

Lee et al. [5] compared three round orifice nozzles with an exit jet Reynolds numbers  $Re_0$  in a range of 10000–30000 and nozzle-to-plate spacing  $H$  in a range  $2D$ – $10D$ , where  $D$  is the exit nozzle diameter. The orifices were square-edged, standard-edged and sharp-edged, respectively. The square-edged orifice is straight hole with straight-through edges ( $90^\circ$  corners at the hole). The standard edged orifice has square edged corners at the entrance, and a bevel edges at the outlet. The sharp-edged orifice is beveled through the entire thickness of the hole (with an angle of  $45^\circ$  relative to the axis normal to the orifice plate). In the stagnation region, the sharp-edged orifice jet yields significantly higher heat transfer rates than either the standard-edged orifice jet or square-edged orifice jet. The effect of nozzle exit configuration on the stagnation point heat transfer is more sensible at shorter nozzle-to-plate spacing.

The literature reveals that for high Reynolds numbers and low nozzle-to-wall distances, two peaks are present on the radial distributions of local Nusselt number, produced by circular impinging jets. The first peak corresponds to the maximum of heat transfer rate and occurs approximately at the nozzle radius. In some investigations [5-8], the location of the first peak is observed from  $r = 0.5D$  to  $r = 0.7D$  for  $H < 4D$ . This peak is attributed to the high turbulence intensity at the nozzle edge and to the direct impingement of large toroidal Kelvin-Helmholtz (K-H) vortices originated in the mixing region. The secondary peak occurs at the radial distance from the stagnation point ranging from  $1.2D$  to  $2.5D$  [5, 7-9]. The second peak is either attributed to the transition from laminar to turbulent boundary layer in the wall jet region [3] or to the unsteady separation of the induced secondary vortices that form near the wall under primary K-H vortices [10]. With the increasing Reynolds number, the location of the secondary peak moves outwards from the stagnation point and the peak height increases [5].

Whereas numerous papers were published on the Nusselt number ( $Nu$ ) distributions generated by impinging jets, only a few studies have been dedicated to the analysis of the corresponding wall shear rate ( $\gamma$ ) distributions [6, 11-13]. Available data of  $Nu$  and  $\gamma$  are compared and reveals similarities in their distributions, on the number of peaks and their radial locations. For high Reynolds number ( $Re_0 = 41600$ )

and  $H < 4D$ , two peaks are evident in  $\gamma$  (or in wall shear stress  $\tau = \mu \cdot \gamma$ ) distribution [12]. Similarly to  $Nu$ -distribution [5-8], the first peak in  $\gamma$ -distribution appears at the distance from the stagnation point ranging from  $r = 0.56D$  to  $r = 0.74D$ , while the second peak is located at  $r = 1.9D$  [12, 14]. The fact that peak-locations in  $\gamma$ -distribution are closely matching with those of  $Nu$ -distribution, suggests that the wall shear stress and the local heat/mass transfer are closely linked. Also, the connection of the heat/mass transfer phenomena with the large-scale structures which develop in the free jet region or with the subsequent flow dynamics in the stagnation and wall jet regions is now recognized [7, 10, 15, 16]. Therefore, the control of large-scale structures in impinging jets is a key element in the strategy of heat/mass transfer optimization and control. The passive control based on nozzle geometry modifications is particularly attractive because of easy implementation in industrial applications.

The present article is in continuation of our previous study in which a round plate orifice jet is compared to a reference convergent nozzle jet in terms of wall shear rate and local mass transfer at a very low Reynolds number,  $Re_0 = 1360$  [17]. It was concluded that the orifice jet enhances significantly transfer phenomenon compared to the reference convergent jet. The orifice jet flow generates larger in size, well-defined and vigorous primary K-H structures with comparison to the convergent nozzle jet. These differences were associated with differences in initial velocity profiles and the resulting flow development. The *vena contracta* in the orifice jet generates a thinner shear layer and an increase of the exit mean velocity relative to exit bulk-velocity.

We consider herein a turbulent case with a Reynolds number  $Re_0 = 5290$ . We also extend the analysis to an innovative geometry of the nozzle, i.e., a round orifice perforated on a hemispherical surface. The hemispherical nozzle has never been used in the literature for jet generation. The hemispherical surface which is supporting the round orifice considered in the present study is intended to increase the stretching of the shear-layer at the jet exit, supposing to generate a more efficient jet dynamics for wall skin friction enhancement. Contrary to previous investigation where the nozzle-to-wall distance was varied in the range  $2D - 5D$ , this distance is now kept constant, i. e.  $H = 2D$  (with  $D = 7.8$  mm for each nozzle). This particular distance was selected by considering that it corresponds approximately to the first half of the potential core length of a round free jet [18], where the K-H toroidal vortices are well formed and are still well defined at the target placed at this distance.

Wall shear stress distribution on the target plate is measured using the electrodiffusion method (ED), the same method as we have used before in [17, 19]. Phares et al. [13] made a critical survey of different techniques used for the measurements of wall shear stress and concluded that the ED method provides the greatest accuracy of any indirect method. To our knowledge, Kataoka et al. [6] have been the first to introduce this technique for the measurement of wall skin friction generated by an impinging jet. This method provides

information on the wall shear rates and the velocity field is captured using Particle Image Velocimetry (PIV). Both techniques (ED and PIV) are complementary as the PIV fails at the vicinity of the wall due to the laser scattering by the solid surface.

The paper is structured within two main Sections. In the Section II we outlined the employed experimental procedures and the Section III is dedicated to results analysis.

## II. EXPERIMENTAL PROCEDURES

### A. Experimental setup and geometry of nozzles

The experiments are conducted in a liquid-liquid jet impinging orthogonally onto a wall. A schematic diagram of its generation in a reservoir is shown in Figure 1. A gear pump (Ismatec with a GJ-N23 head) draws the liquid from a reservoir and delivers it to a nozzle. The liquid jet issued from the nozzle impinges a circular target disc provided with six electrodes (Figure 2) which serve as the probes for electrodiffusion measurements. The temperature of liquid is controlled by a cooling coil within  $\pm 0.2^\circ\text{C}$ . The nozzle is screwed to a 200 mm length stainless steel tube with inner and outer diameters of 15 and 20 mm, respectively. A honeycomb manufactured of a 7 mm thick disc by drilling 17 holes with a diameter of 2 mm was fitted in the tube inlet. The nozzle assembly was located in a support which allowed vertical movement for accurate alignment of the nozzle axis with the electrodes centre. The reservoir was placed on a sliding compound table (Proxxon KT 150) which allowed movement in the axial and transverse direction relative to the nozzle with a precision of 0.05 mm.

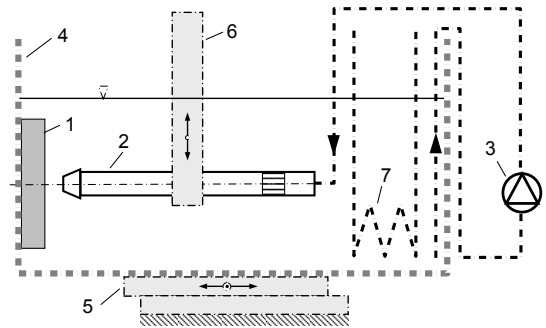


Figure 1: Diagram of apparatus: 1 target disc with electrodes, 2 tube with nozzle and honeycomb, 3 pump, 4 reservoir, 5 compound table, 6 nozzle holder, 7 cooling coil

The target (Figure 2) was manufactured of a Poly(methyl methacrylate) disc with a diameter of 100 mm and a thickness of 17 mm by first drilling holes to insert the electrodes. The platinum foil with a diameter of 50 mm and a thickness of 50  $\mu\text{m}$  was assembled centrally with the disc using Neoprene glue. Holes with a diameter 0.7 mm were drilled through the platinum foil as a continuation of the holes in the disc. The electrodes were manufactured of a 0.5 mm platinum wire

which was coated electrophoretically using a deposit of a polymeric paint. After soldering connecting cables, the electrodes were glued with an epoxy resin into the disc, so that the tops of the platinum wires just projected above the platinum foil. The wires were then rubbed down flush with the surface of the platinum foil using progressively finer grades of emery paper. The last emery paper had a grit size of  $10\ \mu\text{m}$ . The whole surface was then polished using a fine dental paste. The resulting surface roughness was about  $0.11\ \mu\text{m}$  which is much less than the Nernst diffusion layer thickness estimated at  $10\ \mu\text{m}$ .

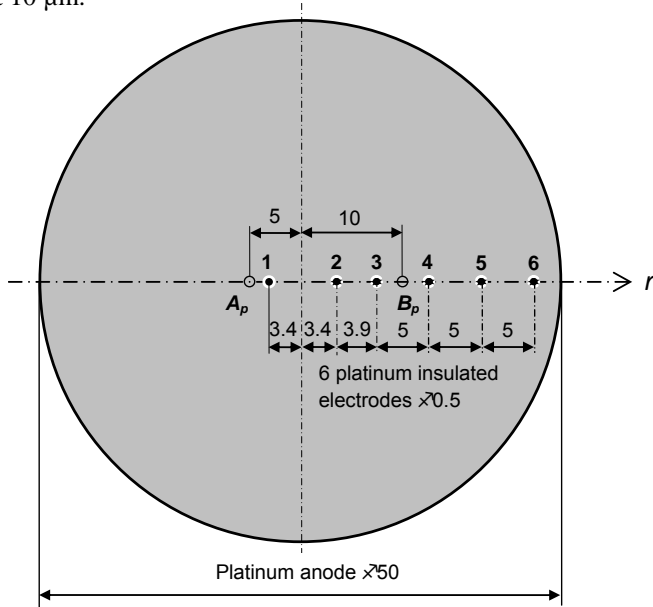


Figure 2: Target disc with electrodes row: 1-6 electrodes  $\phi$  0.5mm.  $A_p$  and  $B_p$  are the limits of stagnation point displacement

In this study, three round nozzles (Figure 3) having the same exit diameter  $D = 7.8\text{mm}$  are compared: a convergent nozzle (CONV in Figure 3 a), a round orifice on a flat plate (RO/P in Figure 3 b) and a round orifice on a hemisphere (RO/H in Figure 3 c). A convergent nozzle had a conical shape with an area contraction 4:1 on a length of 17 mm. The flat surface orifice nozzle (RO/P) is drilled in a metal plate with a thickness of 0.5 mm, while the curve surface orifice nozzle (RO/H) is made in a hollow sphere with an internal radius of 7.6 mm and a thickness of 1 mm.

The Reynolds number based on the diameter  $D$  and the jet bulk-velocity  $W_b$  ( $W_b = 4Q_0/\pi D^2 = 0.72\text{m/s}$ ) was  $Re_b = 5290$ . The distance  $H$  between the jet exit and the target wall was kept constant,  $H = 2D$ , for all the measurements. The coordinate system  $(r, Y, Z)$  attached to the nozzle is shown in Figure 4. As sketched in this figure, the flow field may be divided into several regions. In the neighborhood of the stagnation point  $S$ , the flow spreads in radial directions parallel to the wall. The development of the impinging jet flow field near the wall is typically divided in two regions: the stagnation region associated with the turning of the mean flow,  $r/D < 1$ , and the radial wall jet region,  $r/D > 1$ .

Table 1: Initial conditions of the three studied flows

Nozzle	$W_b$ (m/s)	$Re_b = \frac{W_b D}{\nu}$	$W_0$ (m/s)	$\frac{W_0}{W_b}$	$\frac{(U_{max})^{Peak}}{W_b}$
CONV	0.72	5290	0.82	1.14	0.99
RO / H			1.07	1.49	1.29
RO / P			1.21	1.68	1.44

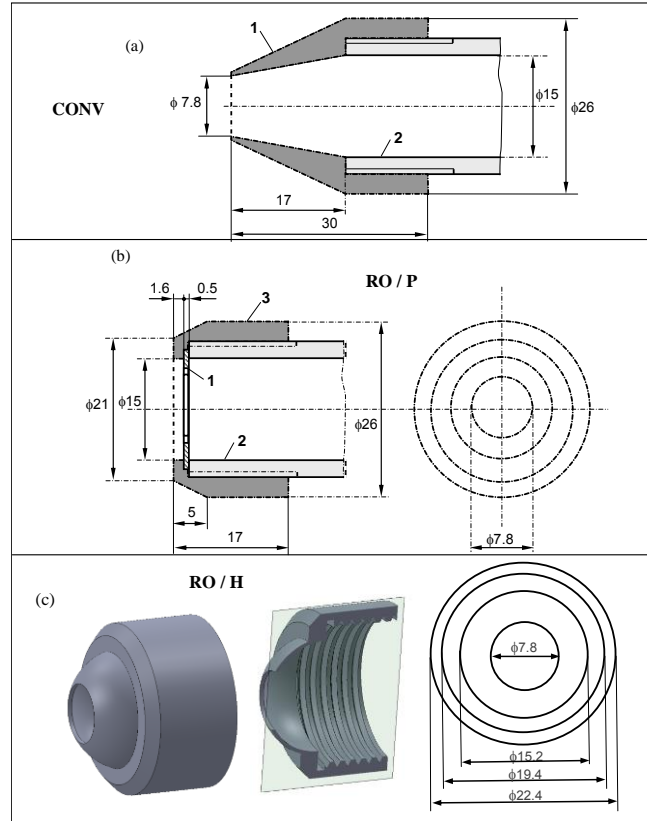


Figure 3: Sketch of nozzles: (a) 1 – Convergent nozzle (CONV), 2 – tube, 3 – sleeve nut; (b) 1– Round Orifice on Plate (RO/P), 2 – tube, 3 – sleeve nut; (c) Round Orifice on Hemisphere (RO/H) – a plane orifice of  $D = 7.8\text{mm}$  is projected onto a spherical surface

### B. PIV measurements

Flow analysis has been carried out using PIV measurements. The PIV system includes a Quantel BigSky 200 mJ dual Yag laser and a FlowSense EO (CCD) camera of  $2048 \times 2048$  pixels resolution with pixel size of  $7.4 \times 7.4\ \mu\text{m}^2$ . The total view field is about  $2D \times 6D$  to cover free and wall jet regions (Figure 4 and Figure 5). The light sheet optics produces a laser sheet of less than 1 mm in thickness. The maximum acquisition frequency of the PIV system is 15 Hz. For each experiment, 500 couples of images are acquired. The recordings are analyzed through two different windows. Firstly, the velocity distribution in the total field of view ( $2D \times 6D$ ) is calculated using an adaptive multi-grid correlation algorithm handling the window distortion and sub-pixel window displacement

(128×128, 64×64, and 32×32 pixels) and 50% overlapping. Secondly, to get a better resolution of velocity vectors in the radial wall jet region (Figure 4) the same algorithm is used with a final grid composed of 8×64 pixels interrogation windows and 50 % overlapping. The prediction-correction validation method of multi-grid algorithm identified on average less than 1% erroneous velocity vectors, which are replaced using a bilinear interpolation scheme. For all the experiments, the uncertainty of the measurement due to the displacement error was estimated to be in the range of 1 to 3 % outside the boundary layer.

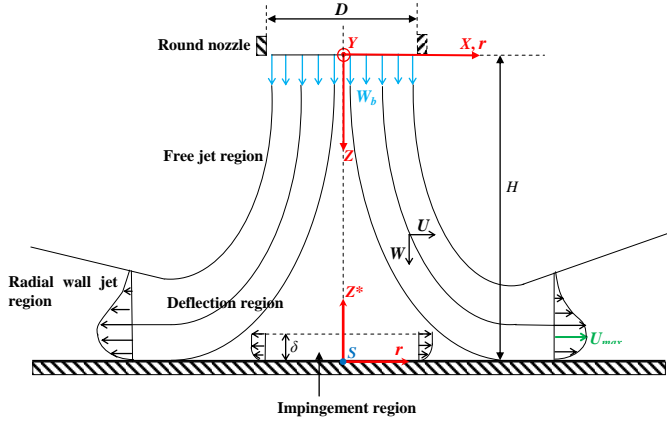


Figure 4: Schematic description of round impinging jet on a flat plate and associated system coordinates. The stagnation point is designated by  $S$

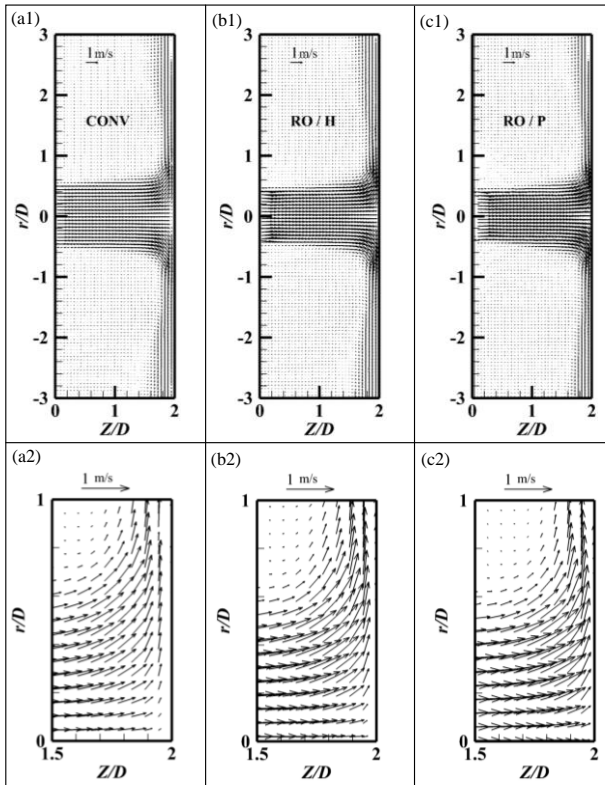


Figure 5: PIV mean field in longitudinal plane  $Y = 0$  of impinging jet: (a) Convergent nozzle (CONV), (b) Round Orifice on Hemisphere (RO / H), (c) Round Orifice on Plane (RO / P); (1) entire field, (2) zoom on deflection region

The uncertainty rises near the impinging plate due to laser scattering, so that the boundary layer is not accessible using PIV technique. This difficulty is bypassed using another measurement technique, which is the electrodiffusion (ED) method described in the next section.

### C. Electrochemical measurements

The electrodiffusion method for wall shear stress measurement consists in using working electrode flush-mounted on the wall to measure the limiting diffusion current. This technique was extensively described in Kristiawan et al. [19], El Hassan et al. [15] and Meslem et al. [17], thus, only a brief summary will be given here. This technique has been developed for measuring the average rates of mass transfer and their fluctuations on a wall. The method is based on electrochemical redox reaction whose rate is very fast but the electric current is limited by the convective mass transfer on the measuring electrode (probe). For the total current through a circular electrode in a viscosimetric flow with a uniform wall-shear rate  $\gamma$ , the formula corresponding to the Leveque's equivalent equation for heat transfer was established by Reiss et al. [20] and is given by:

$$I_L = \frac{0.884\pi}{3^{1/3} \Gamma(4/3)} n F C \gamma^{1/3} D_C^{2/3} R^{5/3} \quad (1)$$

Where  $C$  is the bulk concentration,  $D_C$  the diffusion coefficient of active species,  $F$  the Faraday constant,  $n$  the number of electrons involved in the electrochemical reaction,  $R$  the radius of the electrode and  $\Gamma$  the gamma function.

Let us recall that the basic assumptions for the derivation of the Leveque relationship (Eq.1) is that the probe is in a flow with parallel streamlines and uniform wall-shear rate  $\gamma$ . In the case of impinging jet, the streamlines in the wall vicinity spread radially from the stagnation point  $S$  (Figures 4 and 5) and the wall-shear rate increases with  $r$ . Kristiawan et al. [19] have determined the drawbacks of application of this equation in the stagnation region for an electrode with  $R = 0.25$  mm. At a radial distance  $r = 1$  mm from the stagnation point  $S$ , the authors have found 2.1% error in wall shear rate. Taking into account the others parameters which can affect the wall shear rate, Meslem et al. [17] conclude that the error on the wall shear rate using Eq.1 is less than 5% for  $r \geq 1$  mm.

## III. RESULTS AND DISCUSSION

### A. Flow characteristics

Figure 5 presents velocity field in the longitudinal plane of each round jet. On the bottom of this figure, a zoom on the recirculation region is given for the same window, i.e.  $0 \leq r/D \leq 1$  and  $1.5 \leq Z/D \leq 2.0$ .

The entire fields (Figure 5 a1, b1, and c1) clearly show that the free jet region is more contracted in RO/H and RO/P cases (Figure 5, b1, c1) than in CONV case (Figure 5 a1). From a detailed comparison of the orifice jets, it can be concluded that

the RO/P orifice nozzle generates greater contraction than RO/H orifice nozzle. As shown in Figure 5 a2, b2 and c2, the contracted free jet region leads to a contracted deflection region.

For an axial position  $Z$ , the extent of the radial jet expansion in the free jet region is defined by the jet thickness  $r_{0.1}$ , which is the radial position in the jet where the axial velocity  $W$  takes the value  $0.1W_c$ ;  $W_c$  is the centerline velocity at the same axial position  $Z$ . The streamwise evolution of normalized jet thickness,  $r_{0.1}/D$ , is plotted in Figure 6 for each jet. As expected, the convergent jet is more expanded than the orifice jets. Comparison of the two orifice jets, confirms that the RO/H nozzle attenuates the *vena contracta* effect, which characterizes orifice jets.

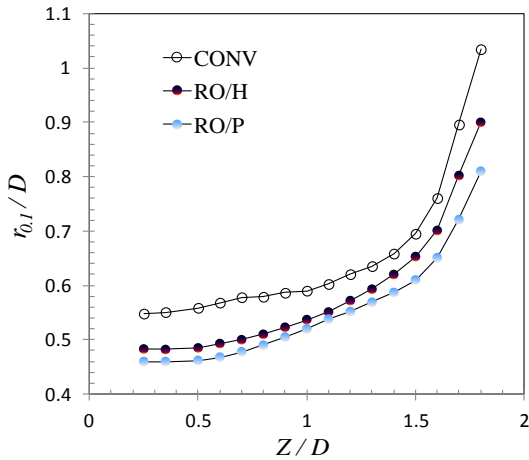


Figure 6: Growth of jet thicknesses in the free jet region

The differences in jet contraction are visible also on the streamwise velocity profiles (Figure 7 a and b), and on transverse velocity profiles as well (Figure 7 c).

In the free jet region, at  $Z = 1.7D$  (Figure 7 b), axial velocity profile exhibits an “M shape”, whereas at  $Z = 0.5D$  (Figure 7 a) the profile is flat. Hence, flow acceleration in the outer edge of the shear layer is a result of jet/wall interaction. Before impinging the wall, the jet accelerates in the outer edge (Figure 7 b) and decelerates on the axis, as visible on streamwise velocity changes along the jet centerline given in Figure 8. As evidenced by this figure, the axial velocity achieves zero at the stagnation point  $S$ . The value of jet bulk velocity  $W_b$  reported in this figure highlights when compared to the maximum centerline velocity  $W_0$ , the level of flow acceleration as a function of nozzle geometry. The most accelerated flow is given by RO/P nozzle, followed by RO/H nozzle and then CONV nozzle (see also Table 1 where the values of  $W_0/W_b$  are provided). The same trend is found in the wall jet region when one compares the changes of maximum velocity  $U_{max}$  along the wall (Figure 9a). Indeed, the peak level of  $U_{max}$  is linked to the jet acceleration level (see Table 1). However, the curves have similar shapes and the position of the peak of  $U_{max}$ ,  $r = 0.95D$ , seems, to be insensitive to the contraction level of the jet flow (Figure 9a). When  $U_{max}$  is normalized by  $W_0$  (Figure 9b), radial distributions of maximum velocity in the wall jet region are self-similar. The comparison of dimensionless distributions

to those of the literature [14, 21, 22] of round jets at the same normalized nozzle-to-plate distance,  $H/D = 2$ , suggests a possible effect of jet exit Reynolds number  $Re_0$  on the level of  $U_{max}/W_0$ . However, the radial position of the peak value remains almost unchanged with different  $Re_0$  and different round nozzle geometries. In fact, the round nozzle in [14, 22] is a long pipe and a convergent nozzle connected to a short pipe in [21].

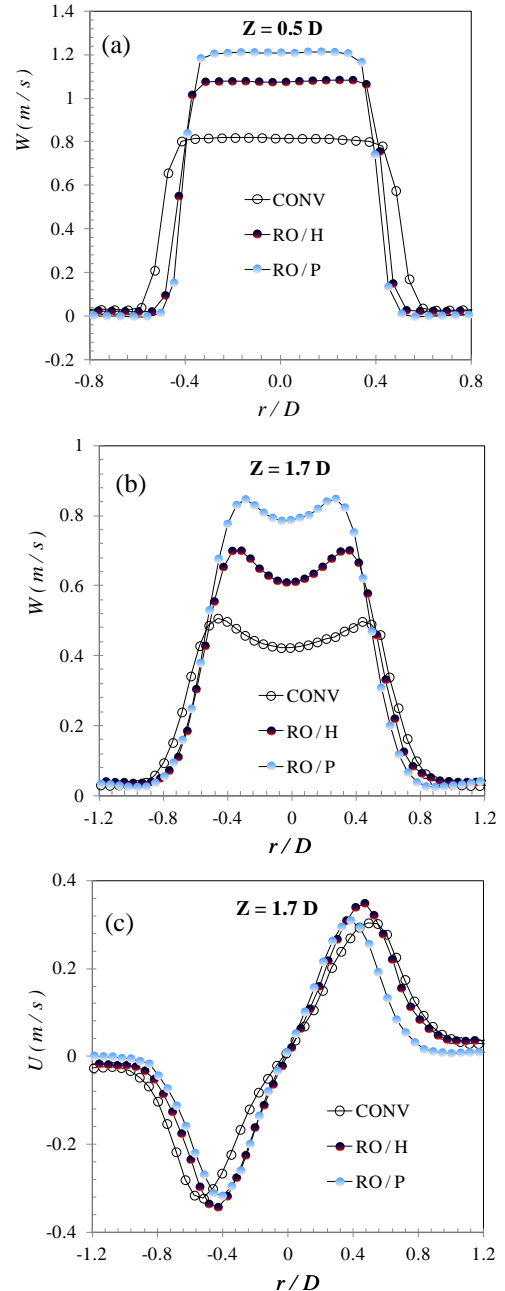


Figure 7: Streamwise velocity (a,b) and transverse velocity (c) profiles in the free jet region

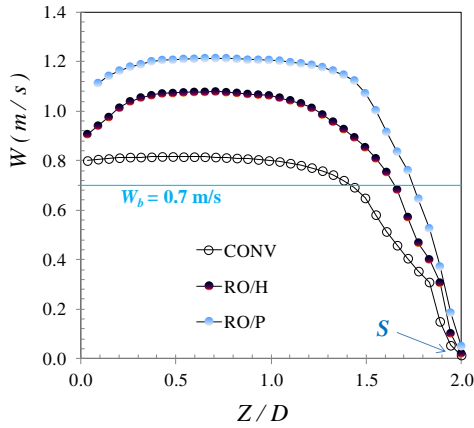


Figure 8: Streamwise mean velocity changes along the jet centerline – comparison to the jet bulk velocity  $W_b$

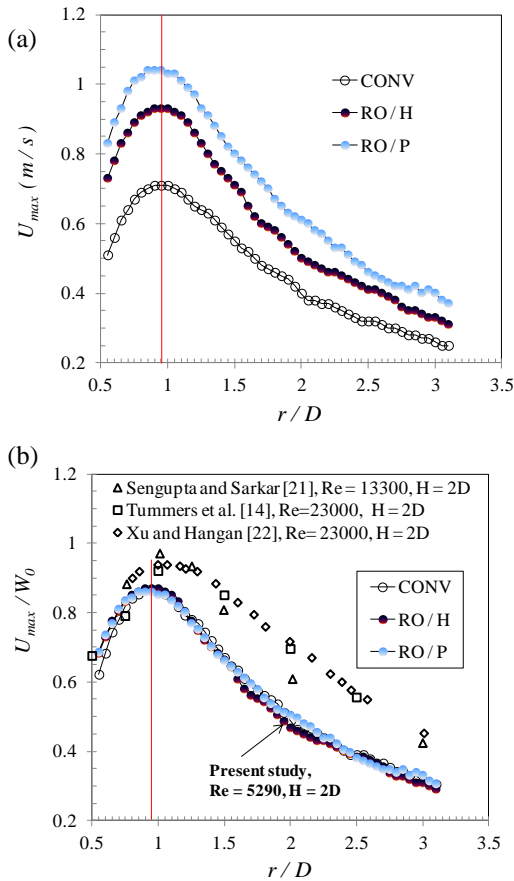


Figure 9: Radial distribution of maximum radial velocity above the wall. (a) dimensional values; (b) dimensionless values and comparison to the literature – the round nozzle in [14, 22] is a pipe and in [21] a convergent connected to a short pipe

### B. Wall shear rate

Local and instantaneous wall shear rate was acquired using the electrodiffusion method (ED) described above in paragraph II.C. To measure the mean and the rms values of the wall shear rate, the signals were recorded with a sampling frequency of 500 Hz during a time of 40 sec.

The radial distributions of the wall shear rate were obtained by moving the stagnation point  $S$  horizontally in the range limited by the points  $A_p$  and  $B_p$  on the target shown in Figure 2. Sixteen displacements of the stagnation point with a step of 1mm were performed to well capture the details of wall shear rate profiles. Thereby, several values of the wall shear rate measured by different electrodes at similar radial distances from the stagnation point were obtained. Based on the comparison of the measured values for a given radial position, it was observed that the repeatability is insured with maximum deviation of  $\pm 5\%$  of the mean value.

The radial distributions of the mean value of wall shear rate  $\gamma$  and its rms  $\sqrt{\gamma'^2}$  are plotted in Figure 10 for CONV, RO/H and RO/P nozzles.

The maximum value of wall shear rate (Figure 10) is equal to  $9880 \text{ s}^{-1}$ ,  $15900 \text{ s}^{-1}$  and  $17000 \text{ s}^{-1}$  for the CONV, RO/H and RO/P nozzle jet, respectively. Hence, the maximum of  $\gamma$  is nozzle geometry dependent and is higher for orifice jet than for convergent jet at  $Re_0=5290$ , as was found earlier for  $Re_0=1360$  [17]. The hemispherical orifice nozzle reduces somewhat  $\gamma_{max}$  level, because the curved surface already converge the flow at the exit and so reduces the *vena contracta* effect. This finding is interesting for applications where wall-friction modulation and hence, local heat/mass transfer control is required. The curvature of the plate supporting the exhaust orifice may be modified to achieve a given level of local friction without changing the volumetric flow rate of the injected fluid.

Figure 11 clearly shows the effect of nozzle geometry on the position of the maximum value  $\gamma_{max}$ . The peak is located at  $r = 0.7D$  for the CONV nozzle jet, and at  $r = 0.6D$  in the RO/H and RO/P nozzle jets. These locations falls in a range of  $0.6D$ - $0.74D$  reported in the literature [11-13] for the round impinging jets when  $H < 4D$ . Thus, the first peak of  $\gamma$  does not coincide with the peak of  $U_{max}$  (Figure 9). The first peak of  $\gamma$  is located in the growth region of  $U_{max}$ .

Figure 11 also highlights what we might call "*the birth of the second peak*" in the region  $r = 1.6D$ - $1.8D$  for both orifice jets. In the convergent jet, this effect is very low suggesting that the second peak is related to the level of  $U_{max}$  in the wall jet region (Figure 9 a), itself related to the velocity acceleration at the jet exit (Figure 8).

The radial distributions of the rms( $\gamma$ ) values are given in Figure 12 in their normalized form. Two peaks are present, although the second peak is fairly attenuated in the convergent jet. The second peak in the rms value is clearly linked to the second peak in the mean value (Figure 11). The first peak in rms distribution (Figure 12) is about  $0.2D$  farther than the first peak in the mean value distribution (Figure 11).

The instantaneous velocity field (Figure 13 a) shows toroidal K-H vortices along the interface between the jet and the surrounding liquid, which subsequently impinges on the target. For brevity, only CONV and RO/H cases are presented.

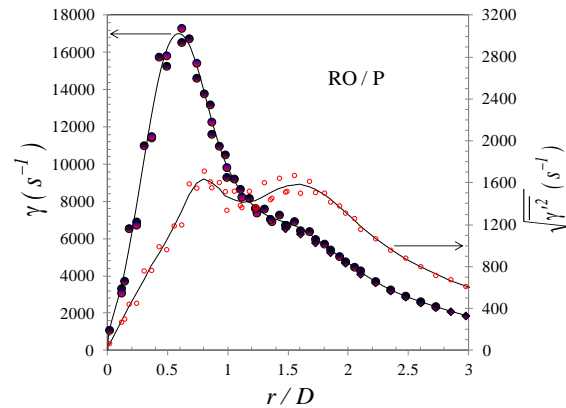
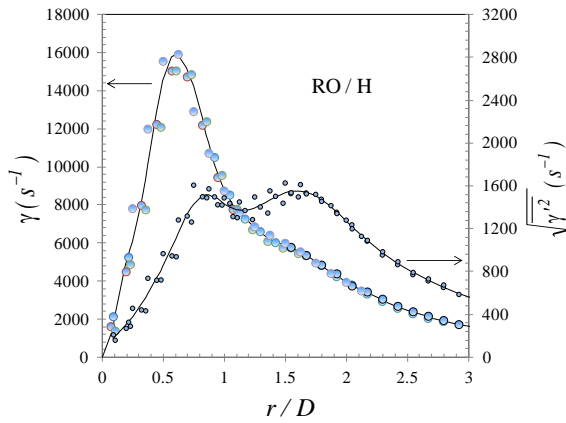
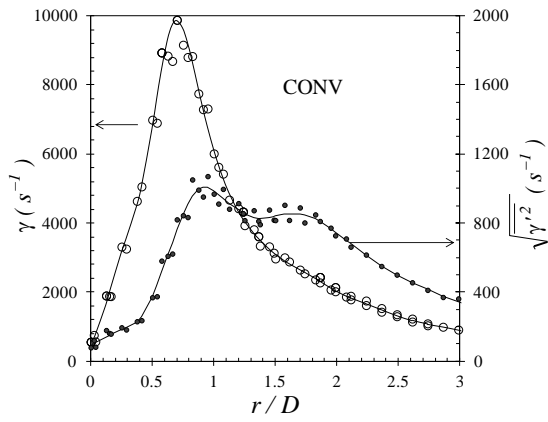


Figure 10: Wall shear rate and its rms values as a function of normalized radial distance from the stagnation point  $S$

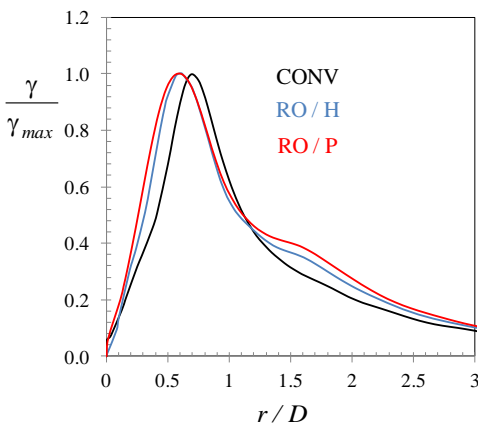


Figure 11: Comparison of normalized wall-shear rate

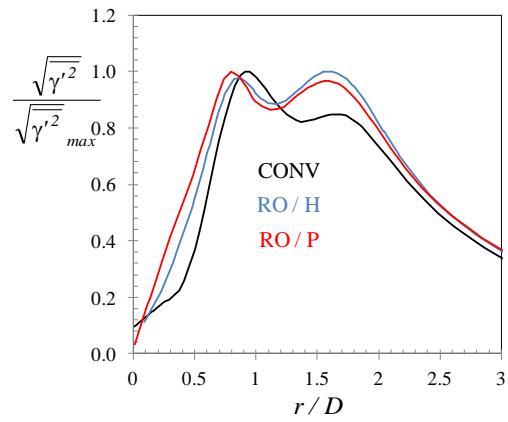


Figure 12: Comparison of normalized values of the rms of wall-shear rate

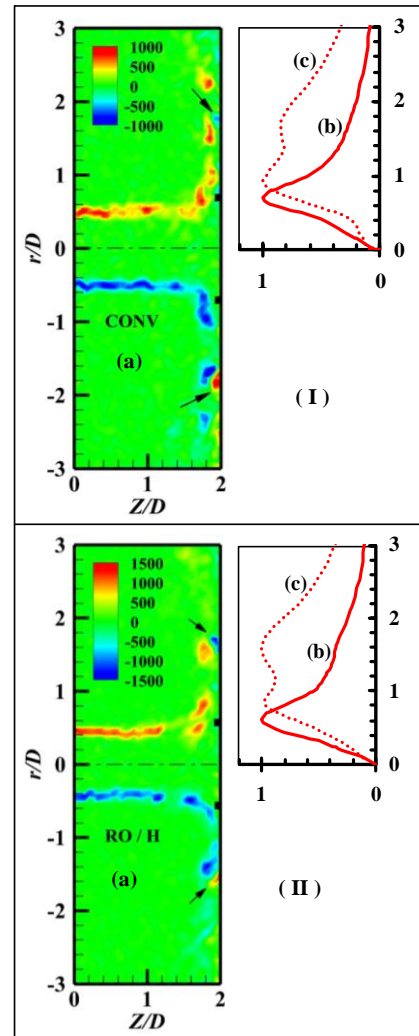


Figure 13: (I) CONV nozzle jet, (II) RO/H nozzle jet: (a) Instantaneous vorticity field  $\omega_\gamma = \frac{\partial U}{\partial Z} - \frac{\partial W}{\partial X}$  - Sticks indicate the position of  $\gamma_{max}$  and arrows indicate secondary vortices on the target; (b)  $\gamma/\gamma_{max}$ ; (c)  $\sqrt{\gamma'^2} / \left(\sqrt{\gamma'^2}\right)_{max}$

The first peak in the distribution of the mean value (Figure 13 b) and in the distribution of the rms value (Figure 13 c), appears in the region where the K-H vortices strike the target (Figure 13 a). The second peak (in  $\gamma$  and in its rms distribution) emerges at the position where appear secondary counter-rotating vortices, designated by an arrow in Figure 13 a. The secondary structures are present in both convergent jet (Figure 13, I) and orifice jet (Figure 13, II).

If we advance once again the similarity between the second peak of  $\gamma$  and the second peak of  $Nu$ , the observation made above is consistent with that of Hadziabdic and Hanjalic [10]. From their LES simulation of a round impinging jet, the authors observed that the second peak in  $Nu$ , (pertinent only for small  $H/D$  and high Reynolds  $Re_0$  numbers) is caused by reattachment of the recirculation bubble and associated turbulence production, as well as subsequent strong advection.

#### IV. Conclusion

Three round impinging jets with a Reynolds number of 5290 and a nozzle-to-wall distance of  $2D$ , have been compared in the present study. A round orifice perforated either on a flat plate (RO/P) or on a hemispherical surface (RO/H), is compared to a reference convergent nozzle (CONV). In each jet, Particle Image velocimetry (PIV) and Electrodiffusion technique (ED) were used to produce a data set on the flow field and the wall shear rate, respectively.

The instantaneous velocity fields indicated that the formation of small secondary vortices above the impingement plate, under primary Kelvin-Helmholtz, occur in the region  $r = 1.6D - 1.8D$ . In the same region, mean and rms values of the wall shear rate exhibited a secondary peak in their radial distributions. The appearance of the secondary peak depends on the level of the maximum radial velocity in the wall-jet region. The level of maximum velocity in the wall jet region is as high as the flow is accelerated at the jet exit. The jet acceleration was shown to be more intensive in the orifice jets than in the convergent jet due to the *vena contracta* effect. However, the curved surface supporting the orifice stretches the flow at the exit, and reduces the *vena contracta* effect. This leads to a lower wall-friction than in the case of the flat orifice. This finding is interesting for applications where wall-friction modulation and hence, local heat/mass transfer control, is required without changing the volumetric flow rate of the injected fluid.

#### ACKNOWLEDGMENT

This work was supported by the Grants of the French National Agency of Research, project "FLUBAT", ANR-12-VBDU-0010 and the Grants of the PRES Limousin Poitou-Charentes

#### REFERENCES

1. Gardon, R., *Heat Transfer Between a Flat Plate and Jets of Air Impinging on It*. Int. Dev. Heat Transfer (ASME), 1962: p. 454-460.

2. Gardon, R. and J.C. Akfirat, *The role of turbulence in determining the heat-transfer characteristics of impinging jets*. international Journal of Heat and Mass Transfer, 1965. **8**: p. 1261-1272.
3. Gardon, R. and J.C. Akfirat, *Heat Transfer Characteristics of Impinging Two-Dimensional Air Jets*. Journal of Heat Transfer, 1966. **88**(1): p. 101-107.
4. Popiel, C.O. and Boguslawski, L. *Effect of Flow Structure on the heat or mass transfer on a Flat plate in Impinging Round jet*. in *2nd UK National Conf. on Heat Transfer*. 1988.
5. Lee, J. and S.J. Lee, *The effect of nozzle configuration on stagnation region heat transfer enhancement of axisymmetric jet impingement*. international Journal of Heat and Mass Transfer, 2000. **43**: p. 3497-3509.
6. Kataoka, K. and Mizushima, T. *Local enhancement of the rate of heat-transfer in an impinging round jet by free-stream turbulence*. in *Heat transfer 1974; Proceedings of the Fifth International Conference, Tokyo, Volume 2*. 1974. Tokyo.
7. Violato, D., et al., *Three-dimensional vortex dynamics and convective heat transfer in circular and chevron impinging jets*. International Journal of Heat and Fluid Flow, 2012. **37**: p. 22-36.
8. Roux, S., et al., *Experimental investigation of the flow and heat transfer of an impinging jet under acoustic excitation*. international Journal of Heat and Mass Transfer, 2011. **54**: p. 3277-3290.
9. Lytle, D. and B.W. Webb, *Air jet impingement heat transfer at low nozzle-plate spacings*. international Journal of Heat and Mass Transfer, 1994. **37**(12): p. 1687-1697.
10. Hadziabdic, M. and K. Hanjalic, *Vortical structures and heat transfer in a round impinging jet*. Journal of Fluid Mechanics, 2008. **596**: p. 221-260.
11. Kataoka, K., et al., *Mass transfer between a plane surface and an impinging turbulent jet: the influence of surface-pressure fluctuations*. Journal of Fluid Mechanics, 1982. **119**: p. 91-105.
12. Alekseenko, S.V. and D.M. Markovich, *Electrodiffusion diagnostics of wall shear stresses in impinging jet*. Journal of Applied Electrochemistry, 1994. **24**: p. 626-631.
13. Phares, D.J., G.T. Smedley, and R.C. Flagan, *The wall shear stress produced by the normal impingement of a jet on a flat surface*. Journal of Fluid Mechanics, 2000. **418**: p. 351-375.
14. Tummers, M.J., J. Jacobse, and S.G.J. Voorbrood, *Turbulent flow in the near field of a round impinging jet*. international Journal of Heat and Mass Transfer, 2011. **54**: p. 4939-4948.
15. El-Hassan, M., et al., *Experimental investigation of the wall shear stress and the vortex dynamics in a circular impinging jet*. Experiments in Fluids, 2012. **52**(6): p. 1475-1489.
16. Hall, J.W. and D. Ewing, *On the dynamics of the large-scale structures in round impinging jets*. Journal of Fluid Mechanics, 2006. **555**: p. 439-458.
17. Meslem, A., et al., *Flow dynamics and mass transfer in impinging circular jet at low Reynolds number. Comparison of convergent and orifice nozzles*. international Journal of Heat and Mass Transfer, 2013. **67**(0): p. 25-45.
18. Rajaratnam, N., *Turbulent jets*. 1976, Amsterdam, Netherlands: Elsevier Scientific Publishing Company.
19. Kristiawan, M., et al., *Wall shear rates and mass transfer in impinging jets: Comparison of circular convergent and cross-shaped orifice nozzles*. international Journal of Heat and Mass Transfer, 2012. **55**: p. 282-293.
20. Reiss, L.P. and T.J. Hanratty, *Measurement of instantaneous rates of mass transfer to a small sink on a wall*. AIChE Journal, 1962. **8**(2): p. 245-247.
21. Sengupta, A. and P.P. Sarkar, *Experimental measurement and numerical simulation of an impinging jet with application to thunderstorm microburst winds*. Journal of Wind Engineering and Industrial Aerodynamics, 2008. **96**(3): p. 345-365.
22. Xu, Z. and H. Hangan, *Scale, boundary and inlet condition effects on impinging jets*. Journal of Wind Engineering and Industrial Aerodynamics, 2008. **96**(12): p. 2383-2402.